


Identifying axion insulator by quantized magnetoelectric effect in antiferromagnetic MnBi₂Te₄ tunnel junction

Yu-Hang Li^{1,*} and Ran Cheng^{1,2,†}

¹Department of Electrical and Computer Engineering, University of California, Riverside, California 92521, USA

²Department of Physics and Astronomy, University of California, Riverside, California 92521, USA

 (Received 22 November 2021; revised 2 February 2022; accepted 23 May 2022; published 28 June 2022)

The intrinsic magnetic topological insulator MnBi₂Te₄ is believed to be an axion insulator in its antiferromagnetic ground state. However, the direct identification of axion insulators remains experimentally elusive because the observed vanishing Hall resistance, while indicating the onset of the axion field, is inadequate to distinguish the system from a trivial normal insulator. Using numerical Green's functions, we theoretically demonstrate the quantized magnetoelectric current in a tunnel junction of atomically thin MnBi₂Te₄ sandwiched between two contacts, which is a smoking-gun signal that unambiguously confirms antiferromagnetic MnBi₂Te₄ to be an axion insulator. Our predictions can be verified directly by experiments.

DOI: [10.1103/PhysRevResearch.4.L022067](https://doi.org/10.1103/PhysRevResearch.4.L022067)

Recently, topological insulators with intrinsic magnetism have become a new frontier, dubbed intrinsic magnetic topological insulators (MTIs), where the time reversal symmetry is broken by spontaneous magnetic ordering rather than magnetic disorders [1–6], holding great potential for the realization of high-temperature topological materials. Since the topological phases of intrinsic MTIs are highly mingled with the magnetic states, manipulating the magnetic ordering through external magnetic fields, temperature, or thickness will simultaneously tune the correlated topological states [7,8]. For example, depending on the magnetic states, MnBi₂Te₄ (MBT) can exhibit versatile topological phases such as topological insulators [9], (high Chern number) Chern insulators [2,10], quantum spin Hall insulators and Weyl semimetals [7], and in particular, axion insulators [11].

Unlike other topological phases characterized by the first Chern number [12,13], an axion insulator is in a higher-order topological phase characterized by the symmetry-protected axion field $\theta = \pi$ [14–17], which can manifest as the quantized topological magnetoelectric (TME) effect [18–20] and other striking transport phenomena [21–25]. However, because the first Chern number of an axion insulator vanishes identically, the ensuing transport effect on a Hall bar device exhibits a vanishing Hall resistance accompanied by a large longitudinal resistance, which is just similar to a normal insulator. This property makes it rather elusive to properly distinguish axion insulators from normal insulators by transport experiments [11]. Therefore, to confirm the existence

of an axion insulator, a viable experimental scheme without ambiguity is needed.

In this Letter, we propose an axion insulator tunnel junction consisting of a few-layer MBT sandwiched between two metallic contacts as an experimental setup to unambiguously identify axion insulators through the quantized TME. We first show that a perpendicular magnetic field can induce a surface charge polarization that is physically related to the layer-resolved Chern numbers and the quantized axion field $\theta = \pi$. When the magnetic field adiabatically varies with time (i.e., with a frequency far less than the insulating gap), the surface charge polarization becomes time dependent and will generate an ac charge current through the tunnel junction. We use the time-dependent nonequilibrium Green's function to quantify the detectable ac current driven by a harmonic magnetic field, which agrees remarkably well with the time derivative of the induced charge polarization, thus strengthening the validity and reliability of our proposed scheme to identify axion insulators. Since archetypal materials parameters have been adopted in the modeling, we anticipate our theory to be able to inspire and guide experiments in the foreseeable future.

Low-energy effective Hamiltonian. MBT is a van der Waals magnet consisting of Te-Bi-Te-Mn-Te-Bi-Te septuple layers (SLs) arranged on a triangle lattice with parallel intralayer ferromagnetic order while adjacent SLs are coupled antiferromagnetically. Under the basis $[|p_z^+, \uparrow\rangle, |p_z^-, \uparrow\rangle, |p_z^+, \downarrow\rangle, |p_z^-, \downarrow\rangle]^T$ with $|p_z^{\pm(\cdot)}\rangle$ the spin- σ orbital of Bi (Te), the low-energy Hamiltonian for a layered MBT can be written as [4,26,27]

$$\mathcal{H} = \sum_{a=0}^3 d_a(\mathbf{k})\Gamma_a + \Delta \sum_i \mathbf{m}_i \cdot \boldsymbol{\sigma} \otimes \tau_0. \quad (1)$$

Here, the first term is an effective Hamiltonian for a three-dimensional topological insulator, where $d_0(\mathbf{k}) = M_0 - B_1 k_z^2 - B_2(k_x^2 + k_y^2)$, $d_1(\mathbf{k}) = A_2 k_x$, $d_2(\mathbf{k}) = A_2 k_y$, $d_3(\mathbf{k}) = A_1 k_z$, with $A_{1(2)}$, $B_{1(2)}$, M_0 being system parameters and the lattice momentum $\mathbf{k} = (k_x, k_y, k_z)$. $\Gamma_0 = \sigma_0 \otimes \tau_3$ and

*yuhang.li@ucr.edu

†rancheng@ucr.edu

Published by the American Physical Society under the terms of the [Creative Commons Attribution 4.0 International](https://creativecommons.org/licenses/by/4.0/) license. Further distribution of this work must maintain attribution to the author(s) and the published article's title, journal citation, and DOI.

TABLE I. Parameters adopted. a_0 is the lattice constant. M_0 , $A_{1(2)}$, and $B_{1(2)}$ are based in Ref. [26]. J , K , and M_S are chosen from Ref. [28]. μ_B is the Bohr magneton. The exchange gap Δ is evaluated from Refs. [29,30].

a_0 (nm)	Δ (eV)	M_0 (eV)	A_1 (eV nm)	A_2 (eV nm)
5	-0.05	-0.1165	0.27232	0.31964
J (meV)	K (meV)	M_S (μ_B)	B_1 (eV nm ²)	B_2 (eV nm ²)
0.68	0.21	5/2	0.119048	0.094048

$\Gamma_a = \sigma_a \otimes \tau_1$ ($a = 1, 2, 3$) where σ_a and τ_a are Pauli matrices acting on the spin and orbital spaces, respectively. The second term describes the exchange interaction between topological electrons and magnetic ordering, where Δ is the exchange strength and \mathbf{m}_i is the unit magnetization vector of the i th SL [4]. Henceforth in all numerical calculations, the materials parameters are shown in Table I, and temperature is set to be zero.

Since the topological states of MBT are intertwined with the magnetic ordering, we first need to determine its magnetic configuration. In the macrospin approximation (spatially uniform magnetization within a particular SL), the magnetic property of an N -SL MBT can be characterized by the free energy [31]

$$U = J \sum_{i=1}^{N-1} \mathbf{m}_i \cdot \mathbf{m}_{i+1} - \sum_{i=1}^N \left[\frac{K}{2} (m_i^z)^2 + M_S \mathbf{B} \cdot \mathbf{m}_i \right], \quad (2)$$

where J is the antiferromagnetic interlayer exchange interaction, K is the easy-axis anisotropy, \mathbf{B} is the external magnetic field, and M_S is the saturation magnetization of each SL. The magnetization vector is parametrized as $\mathbf{m}_i = \{\sin \theta_i \cos \phi_i, \sin \theta_i \sin \phi_i, \cos \theta_i\}$ with θ_i (ϕ_i) the polar (azimuthal) angle. Without losing generality, we assume that \mathbf{B} is applied along the z direction and \mathbf{m}_i rotates only in the xz plane. We obtain the equilibrium magnetic configuration by minimizing the free energy U using the steepest descent method [32], which is detailed in the Supplemental Material (SM) [33].

Figure 1(a) shows the total magnetization as a function of the applied magnetic field for a 6-SL MBT, where we identify the spin-flop critical points at around $B_c^\pm \approx \pm 3$ T, beyond which the Zeeman energy overcomes the exchange and anisotropy interactions and induces noncollinear spin configurations until the system is fully polarized into a ferromagnetic state at above 10 T (see Fig. S1 in the SM). Such a distinct magnetic evolution is in quantitative agreement with experiments [2,11]. The complicated spin configurations in the intermediate spin-flop phases are discussed in the SM [33].

In-plane transport properties on a Hall bar. To study the electronic transport, we first discretize the continuum Hamiltonian Eq. (1) on a cubic lattice ($a_0 = 5$ nm) invoking the $k \cdot p$ perturbation. Then, under a Hall bar device geometry as illustrated in the inset of Fig. 1(a), we calculate the Hall resistivity ρ_{xy} and the longitudinal resistivity ρ_{xx} using the Landauer-Büttiker formula [33,34]. To incorporate fluctuations, we also add a disorder potential $\mathcal{H}_D = V(\mathbf{r})s_z \otimes \sigma_0$ to

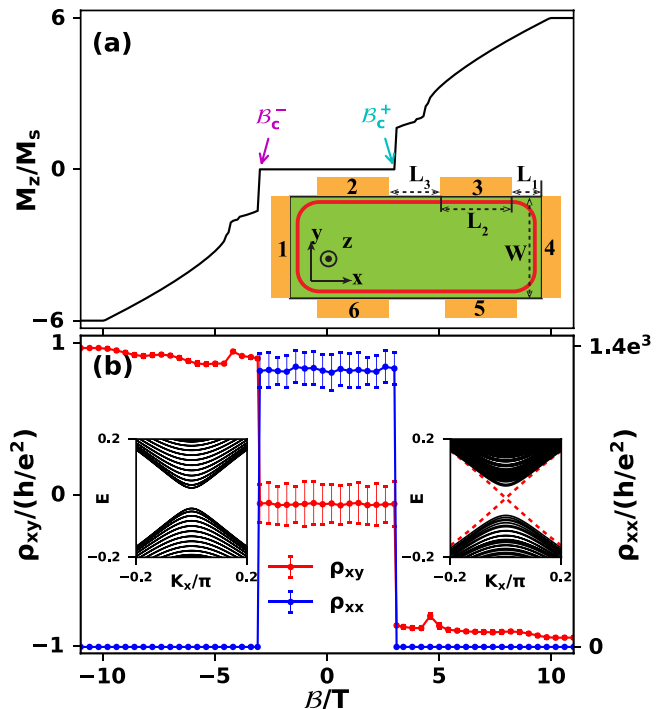


FIG. 1. (a) Total magnetization as a function of magnetic field for a 6-SL MBT. Inset: Schematics of a Hall bar device where the metallic leads are shaded orange and the MBT is colored green. The red curve marks the edge channel when the MBT becomes a Chern insulator (i.e., when $|\mathcal{B}| > |\mathcal{B}_c^\pm|$). (b) Longitudinal resistivity ρ_{xx} and Hall resistivity ρ_{xy} as functions of magnetic field. The data are obtained on a Hall bar of size $L_1 \times L_2 \times L_3 \times W = 5 \times 50 \times 30 \times 50$ with a disorder strength $D = 0.1$ eV (comparable to the magnetic exchange gap) after averaging over 160 computations. Insets: Band structures along the x direction for a 6-SL MBT in its antiferromagnetic (left) and ferromagnetic (right) states.

the lattice Hamiltonian, where $V(\mathbf{r})$ is uniformly distributed within $[-D/2, D/2]$ with D being the disorder strength. The Fermi level is zero as we do not consider doping or gating.

For a 6-SL MBT device reflecting a real experimental setup [11], we obtain ρ_{xx} and ρ_{xy} by averaging 160 repeated calculations, which are plotted as functions of magnetic field \mathcal{B} (along z) in Fig. 1(b). The results show a topological phase transition from a normal insulator (indistinguishable from an axion insulator) with a vanishing Chern number $\mathcal{C} = 0$ at low magnetic fields into a quantum anomalous Hall insulator with $\mathcal{C} = \pm 1$ at high magnetic fields. When $|\mathcal{B}| < \mathcal{B}_c^+$, the magnetic ground state remains antiferromagnetic with antiparallel spins on the adjacent SL, and the system preserves the \mathcal{PT} symmetry. Because the spin flips its sign under \mathcal{PT} operation [$\mathcal{PT}: \mathcal{H}(\mathbf{k}, \uparrow) \rightarrow \mathcal{H}(\mathbf{k}, \downarrow)$], the bands must be doubly degenerate with a band gap of $\delta \approx 2\Delta$ at $k_x = 0$, as shown in the left inset in Fig. 1(b). Consequently, we obtain $\mathcal{C} = 0$, hence a vanishing Hall resistivity and a large longitudinal resistivity akin to a normal insulator. While angle-resolved photoemission spectroscopy (ARPES) experiments showed controversial results on the band gap in MBT [29,35], transport measurements strongly support the existence of large gaps in both the antiferromagnetic and ferromagnetic states of MBT [2,10,11] by confirming the insulating behavior in

longitudinal transport, even though this insulating gap cannot tell axion insulators from normal insulators.

When $|\mathcal{B}|$ exceeds \mathcal{B}_c^+ , however, the magnetic moments undergo a spin-flop transition which breaks the time reversal symmetry for electrons. Correspondingly, the topological Chern number becomes $\mathcal{C} = -\text{sgn}(\mathcal{B})$, leading to a quantized Hall resistivity $\rho_{xy} = h/(Ce^2)$ and a vanishing longitudinal resistivity $\rho_{xx} = 0$ [12]. The deviations of ρ_{xy} around the integer values are ascribed to the finite-size effect, which can be suppressed by enlarging the system size. The in-plane resistivities shown in Fig. 1 agree quantitatively with experimental observations [11,36] widely regarded as evidence of an axion insulator. Nevertheless, the topological phase transition taking place here is inadequate to determine an axion insulator because the $\mathcal{C} = 0$ phase appearing at small fields by itself is indistinguishable from a normal insulator.

Surface charge polarization and layer-resolved Chern numbers. A defining feature of an axion insulator is the topological TME enabled by the quantized θ field, which, unlike the Chern number \mathcal{C} , can uniquely characterize the axion insulator phase. On the one hand, a magnetic field \mathbf{B} below the spin-flop threshold will induce a quantized charge polarization $\mathbf{P} = e^2\theta\mathbf{B}/(2\pi h)$ [14], which is intimately related to the layer-resolved Chern numbers. If the applied \mathbf{B} field is time dependent, a charge current proportional to $d\mathbf{P}/dt$ will be generated, enabling a directly detectable signal to be discussed later. On the other hand, the TME also manifests as the magnetization induced by an electric field [37]. However, the TME coefficient quantized by θ is typically two orders of magnitude smaller than that of ordinary magnetoelectric materials [38]. Therefore, the TME is more amenable to transport measurement as the sensitivity of the detecting current is extremely high. Nonetheless, as a consistency check, we also calculated the tiny magnetization induced by an electric field, which indeed turns out to be quantized by the θ field (see the SM [33]).

To calculate \mathbf{P} , we consider a slab of thickness L_z and widths $L_x = L_y$ with open boundary conditions and assume that a static magnetic field $\mathbf{B} = (0, 0, B)$ is applied along the z direction, which amounts to a magnetic flux of $\Phi_0 = Ba_0^2$ per unit cell. Using the equilibrium Green's function method [33], we obtain the charge distribution $Q(\mathbf{r}) = -e\langle\hat{n}(\mathbf{r})\rangle$, where $-e$ is the electron charge and $\hat{n}(\mathbf{r})$ is the electron density operator. Figure 2 (blue dots) plots the charge distribution among each SL, $Q_z = \sum_{x,y} Q(\mathbf{r})$, with respect to an averaged background charge $\bar{Q}(\mathbf{r}) = \sum_{x,y,z} Q(\mathbf{r})/L_z$ which compensates the positive ions in the lattice. Since $Q(\mathbf{r})$ is an odd function of z , as shown in Fig. 2, there is indeed a finite charge polarization $\mathbf{P} = \int dV \mathbf{r} Q(\mathbf{r})$. As will be shown later, only surface charges contribute to the detectable current, thus only the surface charge polarization $P_z = [Q(L_z/2) - Q(-L_z/2)]/2 - \bar{Q}(\mathbf{r})$ is relevant to our discussion. Ideally, the surface charge polarization P_z should be very close the total polarization P , but finite-size effects can bring about deviations. Fortunately, we find that the finite-size effects are well suppressed by increasing the thickness L_z . It turns out that $P_z(L_z = 6, 8, 10) = 0.91, 0.97, 0.99$ ($e^2\Phi/2h$) with $\Phi = L_x L_y \Phi_0$ being the total magnetic flux penetrating the slab, rapidly approaching the quantized value determined by the axion field $\theta = \pi$.

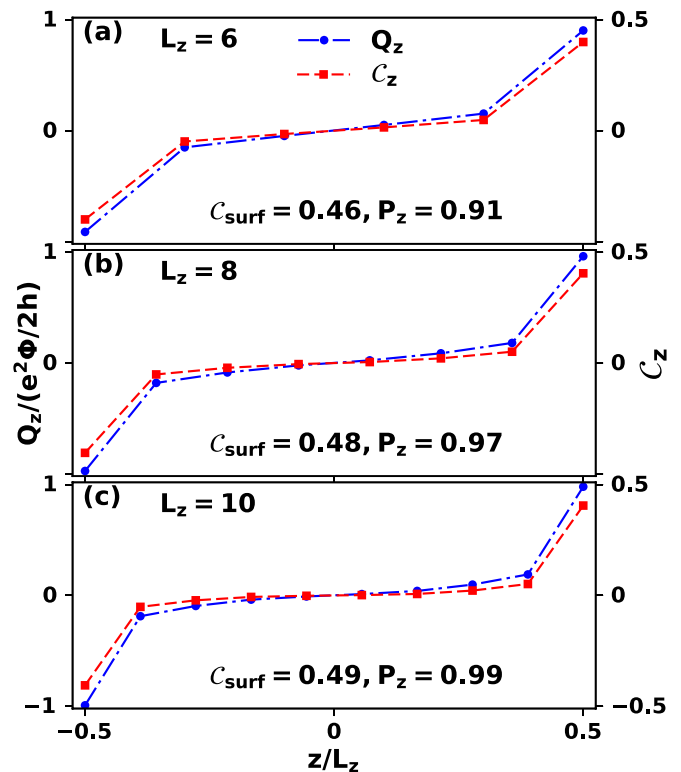


FIG. 2. Charge distribution among each SL relative to the background average $Q_z - \bar{Q}(\mathbf{r})$ (blue dots) and layer-resolved Chern numbers \mathcal{C}_z (red squares) for MBT of thickness (a) $L_z = 6$, (b) $L_z = 8$, and (c) $L_z = 10$ on a slab of size $L_x \times L_y \times L_z$ with $L_x = L_y = 40$. Here, the magnetic flux per unit cell is $\Phi_0 = 0.05h/2e$ and the total magnetic flux is $\Phi = L_x L_y \Phi_0$, which corresponds to a magnetic field of $B = 2$ T smaller than the spin-flop threshold $\mathcal{B}_c \approx 3.0$ T ($a_0 = 5$ nm).

We now turn to the layer-resolved Chern numbers \mathcal{C}_z which reflect the relative contribution to the system topology by different SLs. To this end, we adopt periodic boundary conditions in the lateral dimensions under the same slab geometry used above. While the layer-resolved Chern numbers can be straightforwardly obtained by projecting the wave functions onto each SL [33] in a clean system, here we resort to the noncommutative approach which is able to incorporate disorders [39], $\mathcal{C}_z = -2\pi i \text{Tr}\{\hat{P}[[\hat{x}, \hat{P}], [\hat{y}, \hat{P}]]\hat{P}_z\}$, where \hat{x} (\hat{y}) is the position operator, \hat{P} is the projector onto the occupied bands, $\hat{P}_z \equiv |\psi_z\rangle\langle\psi_z|$ is the projector onto the z th SL, $[\dots]$ is the commutator, and Tr denotes the trace. In the presence of \mathcal{PT} symmetry, \hat{P}_z flips sign on opposite surfaces because $\hat{P}_{-z} = |\psi_{-z}\rangle\langle\psi_{-z}| = \mathcal{PT}|\psi_z\rangle\langle\psi_z|\mathcal{PT} = (\mathcal{PT})^2|\psi_z\rangle\langle\psi_z| = -|\psi_z\rangle\langle\psi_z| = -\hat{P}_z$, ensuring that the layer-resolved Chern numbers are odd in z/L_z .

Figure 2 shows the layer-resolved Chern numbers \mathcal{C}_z with three different thicknesses $L_z = 6, 8, 10$ (red squares), which agree remarkably well with the charge distribution Q_z . Even in the presence of disorders, we find that \mathcal{C}_z and Q_z are very robust (see SM [33]), suggesting that they are topologically protected properties intrinsic to the axion insulator. Correspondingly, the surface Chern number $\mathcal{C}_{\text{surf}}^{L_z} = \sum_{z=-L_z/2}^0 \mathcal{C}_z$ is almost half quantized, $\mathcal{C}_{\text{surf}}^6 = 0.46$, $\mathcal{C}_{\text{surf}}^8 = 0.48$, and $\mathcal{C}_{\text{surf}}^{10} = 0.49$, indicating a distinct bulk axion field $\theta = \pi$ [40].

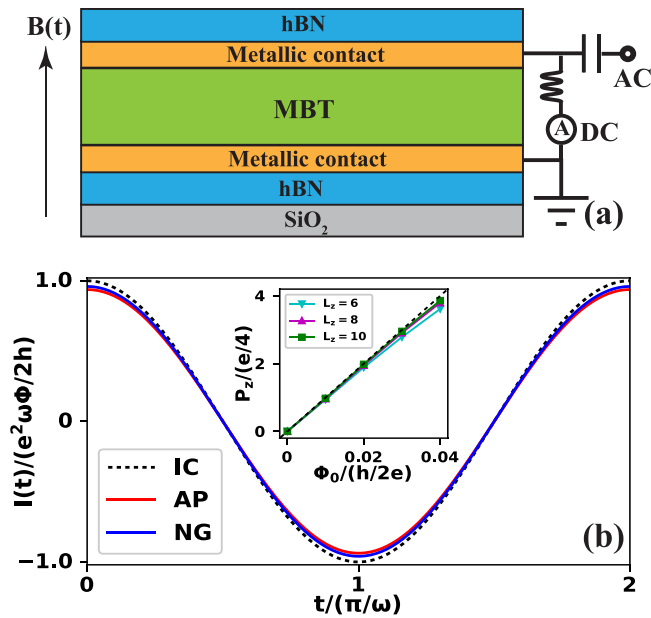


FIG. 3. (a) Schematics of the proposed AITJ setup to detect the dynamical TME. The metallic leads are connected to a bias tee to separate the harmonic ac output from the dc output which is short circuited. The hexagonal boron nitride (hBN) flakes are added to avoid degradation [43], and the whole device is placed on a silicon dioxide substrate. (b) Output current $I(t)$ induced by an ac magnetic field $\hat{z}B \sin \omega t$ calculated by the time-dependent nonequilibrium Green's function (NG) (solid blue), and the adiabatic variation of the surface charge polarization (AP) (solid red), respectively. The ideal case (IC) (dotted black) for an exactly quantized axion field $\theta = \pi$ is plotted as a reference. System size: $L_x = L_y = 20$ and $L_z = 6$. Magnetic flux per unit cell: $\Phi_0 = 0.05h/2e$. Driving frequency: $\hbar\omega = 0.001$ eV. Inset: Surface charge polarization as a function of the magnetic flux for three different thicknesses $L_z = 6, 8, 10$.

Charge current in MBT tunnel junction. To detect the quantized TME in MBT using a transport experiment, we need to consider a time-dependent magnetic field such that the induced surface charge polarization becomes dynamical and produces a charge current in the z direction. This approach has been utilized to characterize multiferroic materials exhibiting nonquantized magnetoelectric effects [38]. To this end, we conceive an axion insulator tunnel junction (AITJ) consisting of an even-SL MBT sandwiched between two metallic contacts [41] as illustrated in Fig. 3(a). In the adiabatic limit, the charge polarization follows the magnetic field at any instant of time, which can be detected directly as an ac output signal from the AITJ. Since the metallic contacts are connected only to the top and bottom layers, only the surface polarization P_z is relevant to the transport measurement.

Using the lattice Hamiltonian, we resort to the time-dependent nonequilibrium Green's function to compute the output current in the AITJ [33]. A harmonic magnetic field $\mathbf{B}(t) = \hat{z}B \sin \omega t$ applied to the AITJ converts to a phase $\Phi_0(t) = \Phi_0 \sin \omega t$ for electrons, where $\Phi_0 = Ba_0^2$ is the magnetic flux per unit cell. As a result, the effective Hamiltonian acquires a time-dependent perturbation that drives the electron motion, forming a charge current. Since the system is now periodic in time, the induced charge current can be expanded

into a Fourier series as [33,42]

$$I(t) = \sum_{n=-\infty}^{\infty} I_n e^{in\omega t}, \quad (3)$$

where I_n is the n th harmonic component satisfying $I_n = -I_{-n}^*$, ensuring a real current. The total current $I(t)$ includes a dc component I_0 and a series of ac components $I_{n>0}$. Truncating the Green's function at order $n = 4$ suffices to yield a converging result [33]. Figure 3(b) (solid blue curve) plots the numerical result of $I(t)$ for one period of oscillation, where the first-order term $I_{n=\pm 1}$ indeed dominates all other components. The plot is offset by I_0 because this dc component is short circuited via the bias tee illustrated in Fig. 3(a).

As an independent confirmation, we use the same harmonic field $\mathbf{B}(t) = \hat{z}B \sin \omega t$ in the surface charge polarization P_z and calculate the resulting charge current $I_z(t) = dP_z(t)/dt$ [44], assuming an adiabatic condition that \mathbf{P} undergoes a quasistatic variation without interband transitions induced by the oscillating $\mathbf{B}(t)$ [45]. Figure 3(b) (solid red curve) plots $I_z(t)$ within one period of oscillation for the same MBT slab, which agrees remarkably well with the harmonic signal $I(t)$ obtained by the nonequilibrium Green's function method. To benchmark the accuracy of our numerical results, we also plot the ideal case for an infinite system, where $I(t) = dP(t)/dt = \theta e^2 / (2\pi\hbar) \omega \Phi \cos \omega t$ with a strictly quantized axion field $\theta = \pi$ [dotted black curve in Fig. 3(b)]. We see that our numerical results obtained both from the nonequilibrium Green's functions and from $P_z(t)$ only slightly deviate from the ideal case, which demonstrates the validity and reliability of our proposal. We mention in passing that if the Fermi level is tuned into the conducting band (e.g., by gating the device [46]), the MBT will become metallic and the induced ac current will vanish.

For an MBT of size $L_x = L_y = 10 \mu\text{m}$, a harmonic magnetic field of strength $B \sim 100$ Gs and frequency $\omega/2\pi = 1$ GHz induces an output ac current $I \sim 1.1$ nA, which is a conservative estimation. Since I scales as $\omega B L_x L_y$, the output current can be amplified by increasing the driving frequency ω , the magnetic field B , or the system size in the lateral dimensions. In the ideal case, the induced surface charge polarization P_z should scale linearly with the magnetic flux per unit cell Φ_0 . To evaluate potential deviations due to finite-size effects, we plot P_z as a function of Φ_0 for different thicknesses against the ideal scaling in the inset of Fig. 3(b), where the finite-size effects turn out to be negligible, further confirming the validity of our calculations.

In summary, we have theoretically proposed an experimental setup to unambiguously identify antiferromagnetic MBT as an axion insulator by detecting the ac current induced by a harmonic magnetic field under the adiabatic condition. Comparing to the vanishing Hall resistance measured in previous experiments, which is inadequate to confirm the axion insulator phase, our proposed scheme provides a smoking-gun signal to identify MBT as an axion insulator.

This work is supported by the Air Force Office of Scientific Research under Grant No. FA9550-19-1-0307. We acknowledge helpful discussions with Chong Wang and U. K. Rößler.

- [1] Y. Tokura, K. Yasuda, and A. Tsukazaki, Magnetic topological insulators, *Nat. Rev. Phys.* **1**, 126 (2019).
- [2] Y. Deng, Y. Yu, M. Z. Shi, Z. Guo, Z. Xu, J. Wang, X. H. Chen, and Y. Zhang, Quantum anomalous Hall effect in intrinsic magnetic topological insulator MnBi_2Te_4 , *Science* **367**, 895 (2020).
- [3] H. Li, S. Y. Gao, S. F. Duan, Y. F. Xu, K. J. Zhu, S. J. Tian, J. C. Gao, W. H. Fan, Z. C. Rao, J. R. Huang, J. J. Li, D. Y. Yan, Z. T. Liu, W. L. Liu, Y. B. Huang, Y. L. Li, Y. Liu, G. B. Zhang, P. Zhang, T. Kondo, S. Shin, H. C. Lei, Y. G. Shi, W. T. Zhang, H. M. Weng, T. Qian, and H. Ding, Dirac Surface States in Intrinsic Magnetic Topological Insulators EuSn_2As_2 and $\text{MnBi}_{2n}\text{Te}_{3n+1}$, *Phys. Rev. X* **9**, 041039 (2019).
- [4] Y.-H. Li and R. Cheng, Spin Fluctuations in Quantized Transport of Magnetic Topological Insulators, *Phys. Rev. Lett.* **126**, 026601 (2021).
- [5] H. Li, H. Jiang, C.-Z. Chen, and X. C. Xie, Critical Behavior and Universal Signature of an Axion Insulator State, *Phys. Rev. Lett.* **126**, 156601 (2021).
- [6] Z. D. Song, B. Lian, R. Queiroz, R. Ilan, B. A. Bernevig, and A. Stern, Delocalization Transition of a Disordered Axion Insulator, *Phys. Rev. Lett.* **127**, 016602 (2021).
- [7] J. Li, Y. Li, S. Du, Z. Wang, B.-L. Gu, S.-C. Zhang, K. He, W. Duan, and Y. Xu, Intrinsic magnetic topological insulators in van der Waals layered MnBi_2Te_4 -family materials, *Sci. Adv.* **5**, eaaw5685 (2019).
- [8] M. Gu, J. Li, H. Sun, Y. Zhao, C. Liu, J. Liu, H. Lu, and Q. Liu, Spectral signatures of the surface anomalous Hall effect in magnetic axion insulators, *Nat. Commun.* **12**, 3524 (2021).
- [9] Y. Gong *et al.*, Experimental realization of an intrinsic magnetic topological insulator, *Chin. Phys. Lett.* **36**, 076801 (2019).
- [10] J. Ge *et al.*, High-Chern-number and high-temperature quantum Hall effect without Landau levels, *Natl. Sci. Rev.* **7**, 1280 (2020).
- [11] C. Liu *et al.*, Robust axion insulator and Chern insulator phases in a two-dimensional antiferromagnetic topological insulator, *Nat. Mater.* **19**, 522 (2020).
- [12] D. J. Thouless, M. Kohmoto, M. P. Nightingale, and M. den Nijs, Quantized Hall Conductance in a Two-Dimensional Periodic Potential, *Phys. Rev. Lett.* **49**, 405 (1982).
- [13] M. Z. Hasan and C. L. Kane, Colloquium: Topological insulators, *Rev. Mod. Phys.* **82**, 3045 (2010).
- [14] X.-L. Qi, T. L. Hughes, and S.-C. Zhang, Topological field theory of time-reversal invariant insulators, *Phys. Rev. B* **78**, 195424 (2008).
- [15] X.-L. Qi and S.-C. Zhang, Topological insulators and superconductors, *Rev. Mod. Phys.* **83**, 1057 (2011).
- [16] R.-X. Zhang, F. Wu, and S. Das Sarma, Möbius Insulator and Higher-Order Topology in $\text{MnBi}_{2n}\text{Te}_{3n+1}$, *Phys. Rev. Lett.* **124**, 136407 (2020).
- [17] Y. Xu, Z. Song, Z. Wang, H. Weng, and X. Dai, Higher-Order Topology of the Axion Insulator EuIn_2As_2 , *Phys. Rev. Lett.* **122**, 256402 (2019).
- [18] A. Sekine and K. Nomura, Axion electrodynamics in topological materials, *J. Appl. Phys.* **129**, 141101 (2021).
- [19] Y. Zhao and Q. Liu, Routes to realize the axion-insulator phase in $\text{MnBi}_2\text{Te}_4(\text{Bi}_2\text{Te}_3)_n$ family, *Appl. Phys. Lett.* **119**, 060502 (2021).
- [20] D. M. Nenko, C. A. C. Garcia, J. Gooth, C. Felser, and P. Narang, Axion physics in condensed-matter systems, *Nat. Rev. Phys.* **2**, 682 (2020).
- [21] L. Wu, M. Salehi, N. Koirala, J. Moon, S. Oh, and N. P. Armitage, Quantized Faraday and Kerr rotation and axion electrodynamics of a 3D topological insulator, *Science* **354**, 1124 (2016).
- [22] W.-K. Tse and A. H. MacDonald, Giant Magneto-Optical Kerr Effect and Universal Faraday Effect in Thin-Film Topological Insulators, *Phys. Rev. Lett.* **105**, 057401 (2010).
- [23] K. Nomura and N. Nagaosa, Surface-Quantized Anomalous Hall Current and the Magnetoelectric Effect in Magnetically Disordered Topological Insulators, *Phys. Rev. Lett.* **106**, 166802 (2011).
- [24] X.-L. Qi, R. Li, J. Zang, and S.-C. Zhang, Inducing a magnetic monopole with topological surface states, *Science* **323**, 1184 (2009).
- [25] A. Y. Gao *et al.*, Layer Hall effect in a 2D topological axion antiferromagnet, *Nature (London)* **595**, 521 (2021).
- [26] D. Zhang, M. Shi, T. Zhu, D. Xing, H. Zhang, and J. Wang, Topological Axion States in the Magnetic Insulator MnBi_2Te_4 with the Quantized Magnetoelectric Effect, *Phys. Rev. Lett.* **122**, 206401 (2019).
- [27] B. Lian, Z. Liu, Y. Zhang, and J. Wang, Flat Chern Band from Twisted Bilayer MnBi_2Te_4 , *Phys. Rev. Lett.* **124**, 126402 (2020).
- [28] S. Yang, X. Xu, Y. Zhu, R. Niu, C. Xu, Y. Peng, X. Cheng, X. Jia, Y. Huang, X. Xu, J. Lu, and Y. Ye, Odd-Even Layer-Number Effect and Layer-Dependent Magnetic Phase Diagrams in MnBi_2Te_4 , *Phys. Rev. X* **11**, 011003 (2021).
- [29] M. M. Otrokov *et al.*, Prediction and observation of an antiferromagnetic topological insulator, *Nature (London)* **576**, 416 (2019).
- [30] A. Zeugner *et al.*, Chemical aspects of the candidate antiferromagnetic topological insulator MnBi_2Te_4 , *Chem. Mater.* **31**, 2795 (2019).
- [31] D. L. Mills, Surface Spin-Flop State in a Simple Antiferromagnet, *Phys. Rev. Lett.* **20**, 18 (1968); D. L. Mills and W. M. Saslow, Surface effects in the Heisenberg antiferromagnet, *Phys. Rev.* **171**, 488 (1968).
- [32] U. K. Rößler and A. N. Bogdanov, Magnetic states and reorientation transitions in antiferromagnetic superlattices, *Phys. Rev. B* **69**, 094405 (2004); Spin-flop transition in antiferromagnetic multilayers, [arXiv:cond-mat/0605493](https://arxiv.org/abs/cond-mat/0605493).
- [33] See Supplemental Material at <http://link.aps.org/supplemental/10.1103/PhysRevResearch.4.L022067> for the lattice Hamiltonian, magnetic configurations, disorder effect, electric field induced magnetization, and all numerical details.
- [34] S. Datta, *Electronic Transport in Mesoscopic Systems*, Cambridge Studies in Semiconductor Physics and Microelectronic Engineering (Cambridge University Press, Cambridge, UK, 1995).
- [35] A. M. Shikin *et al.*, Nature of the Dirac gap modulation and surface magnetic interaction in axion antiferromagnetic topological insulator MnBi_2Te_4 , *Sci. Rep.* **10**, 13226 (2020).
- [36] J. Cai *et al.*, Electric control of a canted-antiferromagnetic Chern insulator, *Nat. Commun.* **13**, 1668 (2022).
- [37] N. Pournaghavi, A. Pertsova, A. H. MacDonald, and C. M. Canali, Nonlocal sidewall response and deviation from exact quantization of the topological magnetoelectric effect in axion-insulator thin films, *Phys. Rev. B* **104**, L201102 (2021).

- [38] C.-W. Nan, M. Bichurin, S. Dong, D. Viehland, and G. Srinivasan, Multiferroic magnetoelectric composites: Historical perspective, status, and future directions, *J. Appl. Phys.* **103**, 031101 (2008).
- [39] E. Prodan, Disordered topological insulators: A non-commutative geometry perspective, *J. Phys. A: Math. Theor.* **44**, 113001 (2011); Quantum transport in disordered systems under magnetic fields: A study based on operator algebras, *Appl. Math. Res. eXpress* **2013**, 176 (2013).
- [40] A. M. Essin, J. E. Moore, and D. Vanderbilt, Magnetoelectric Polarizability and Axion Electrodynamics in Crystalline Insulators, *Phys. Rev. Lett.* **102**, 146805 (2009).
- [41] In artificial heterostructures involving 2D materials, graphene contacts are preferred (see, for example, Refs. [43,46]) because they can be incorporated without the need for lattice matching.
- [42] Y.-H. Li, J. Song, J. Liu, H. Jiang, Q.-F. Sun, and X. C. Xie, Doubled Shapiro steps in a topological Josephson junction, *Phys. Rev. B* **97**, 045423 (2018).
- [43] T. Song *et al.*, Giant tunneling magnetoresistance in spin-filter van der Waals heterostructures, *Science* **360**, 1214 (2018).
- [44] R. D. Li, J. Wang, X. L. Qi, and S. C. Zhang, Dynamical axion field in topological magnetic insulators, *Nat. Phys.* **6**, 284 (2010).
- [45] So long as the driving frequency $\hbar\omega$ is far less than the band gap Δ of the MBT, we can treat the magnetic field as varying adiabatically. The driving frequency of the magnetic field $\hbar\omega$ is on the order of μeV , which is indeed far less than the energy gap $\Delta \sim 100 \text{ meV}$.
- [46] S. Jiang, J. Shan, and K. F. Mak, Electric-field switching of two-dimensional van der Waals magnets, *Nat. Mater.* **17**, 406 (2018).